

The role of magnetic boundaries in kinematic and self-consistent magnetohydrodynamic simulations of precession-driven dynamo action in a closed cylinder.

André Giesecke,¹ Mike Wilbert,² Ján Šimkanin,³ Rainer Grauer,² and Frank Stefani⁴

¹*Institute of Fluid Dynamics, Helmholtz-Zentrum Dresden-Rossendorf, Bautzner Landstrasse 400, D-01328 Dresden, Germany*

²*Institut für theoretische Physik I, Ruhr Universität Bochum, D-44780 Bochum, Germany*

³*Institute of Geophysics, Czech Academy of Sciences, Boční II/1401, 141 00 Prague 4 – Spořilov, Czech Republic^{a)}*

⁴*Institute of Fluid Dynamics, Helmholtz-Zentrum Dresden-Rossendorf, Bautzner Landstrasse 400, D-01328 Dresden, Germany*

(*Electronic mail: grauer@rub.de)

(*Electronic mail: jano@ig.cas.cz)

(*Electronic mail: mike.wilbert@rub.de)

(*Electronic mail: a.giesecke@hzdr.de)

(Dated: 28 October 2024)

We numerically examine dynamo action generated by a flow of an electrically conducting fluid in a precessing cylindrical cavity. We compare a simplified kinematic approach based on the solution of the magnetic induction equation with a prescribed velocity field with the results from a self-consistent three-dimensional simulation of the complete set of magnetohydrodynamic equations. The different kinematic models show a strong influence of the electromagnetic properties of outer layers, which manifests itself in the existence of two different branches with dynamo action. In all cases, we observe a minimum for the onset of dynamo action in a transitional regime, within which the hydrodynamic flow undergoes a change from a large-scale to a more small-scale, turbulent behaviour. However, significant differences in the absolute values for the critical magnetic Reynolds number occur, and they can be explained by the low rotation rate in the MHD simulations achievable for technical reasons. In these models the character of the dynamo solution is small-scale and the magnetic energy remains significantly smaller than the kinetic energy of the flow. In irregular intervals, we observe dynamo bursts with a local concentration of the magnetic field, resulting in a global increase of the magnetic energy by a factor of 3 to 5. However, diffusion of the local patches caused by strong local shear is too rapid, causing these features to exist for only a short period (i.e., shorter than a rotation period) so that their dynamical impact on the dynamo remains small. As the magnetic field is small-scale and weak, the nonlinear feedback on the flow through the Lorentz force remains small and arises essentially in terms of a slight damping of the fast timescales, whereas there is no noticeable change in flow amplitude compared to the hydrodynamic case.

^{a)}Also at Institute of Fluid Dynamics, Helmholtz-Zentrum Dresden-Rossendorf, Bautzner Landstrasse 400, D-01328 Dresden, Germany.

I. INTRODUCTION

The experimental investigation of magnetic field generation through a flow of electrically conductive fluid is of great interest, as such a dynamo process is crucial for many astrophysical bodies and allows conclusions to be drawn about their evolution and internal structure. Following the successful first-generation dynamo experiments in Karlsruhe¹ and Riga², which confirmed the fundamental principle, and subsequent dynamo experiments in Cadarache³, characterized by a wide variety of different dynamic behaviours, a new experiment is currently being set up at HZDR^{4,5}. In this experiment, a flow of liquid sodium in a precessing cylinder is intended to generate a magnetic field. A mechanical drive such as precession is indeed capable of generating strong flows, allowing for the large flow amplitudes required for the occurrence of the dynamo effect. This contrasts with potentially more straightforward mechanisms, such as convection, which at typical laboratory scales may not achieve sufficiently vigorous flows due to lower driving efficiency. In addition, precession as a flow drive makes perfect sense in a dynamo experiment because driving on the largest possible length scale – the size of the container – opens up significantly more degrees of freedom for establishing a (turbulent) flow through cascade processes than in the case of the previously highly optimized experiments⁶.

Precession is a repeatedly proposed driving mechanism for natural dynamos, whether for Earth⁷ or the Moon⁸. Paleomagnetic records suggest that the geodynamo was active even before the formation of the Earth’s solid inner core, which implies that thermochemical convection, driven by the cooling and crystallization of the core, was not always the primary mechanism. Before the onset of thermochemical convection, alternative mechanisms must have driven the early geodynamo. Among the most plausible candidates are precession-driven and tide-driven flows, which could have provided the necessary energy for maintaining the magnetic field in the Earth’s early history. This follows from recent experiments and numerical computation yield rather large values for the heat conductivity under conditions typical for the Earth’s liquid core, which imposes strict energetic constraints for the convective state, particularly for the early geodynamo (before the formation of the solid inner Earth’s core, see e.g. Olson⁹, Landeau *et al.*¹⁰). While it is relatively clear that the laminar flow directly driven by precession is energetically insignificant¹¹, the original idea of Malkus was based on a turbulent base state⁷, which was underpinned by estimates of an upper limit

to (viscous) dissipation by Kerswell¹². Indeed, precession-driven fluid flows exhibit several instabilities, allowing both forward and backward cascades of energy transfer¹³ that end up in a flow state with small-scale turbulence superimposed by large-scale flow contributions essentially in terms of a circulation opposite to the original rotation of the container^{14,15}.

Regarding the Lunar dynamo, which around 4 billion years ago generated a magnetic field of comparable strength to that of today's Earth, precession is indeed the most promising candidate to explain the observations including the disappearance of the dynamo about 3 billion years ago, see e.g. Stys and Dumberry¹⁶.

Precession-driven dynamos have been the subject of numerous numerical studies, and there are now successful dynamo simulations in all conceivable geometries, including spheres¹⁷, spheroids¹⁸, cylinders¹⁹, or cubes²⁰. A preliminary experiment with sodium in a precessing cylinder was conducted in the early 1970s²¹. This experiment demonstrated the amplification of an externally applied magnetic field by a factor of three, however, the setup at that time was not large enough to achieve the magnetic Reynolds numbers required for a dynamo.

Preliminary investigations using a kinematic model based on the geometry of the planned experiment and the large-scale flow from hydrodynamic simulations showed that the dynamo effect works best in the narrow transition region that separates the subcritical from the supercritical state^{4,22}. In the present study, we deepen the investigation of the dynamo effect in the transitional regime and furthermore, we investigate the influence of the magnetic boundary conditions and turn to full self-consistent models to study the influence of the nonlinear terms and the Lorentz force feedback on the flow.

The present study is organized as follows. In section II A, we introduce the equations that describe an electrically conducting fluid flow in a precessing cylinder and the related magnetic induction. We further summarize the essential response of the fluid to the forcing imposed by the precession of the container and present the evolution when increasing this forcing. The subsequent section II C is dedicated to the results obtained from kinematic dynamo models, where only the induction equation is solved numerically assuming a prescribed, time-independent flow. In this section, we detail the impact of the electrical conductivity of the container. Section III focuses on the corresponding results of the full set of magneto-hydrodynamic (MHD) equations and reveals differences and similarities with the kinematic dynamo. We end our study with the conclusions in section IV, where we try to adopt our results for the forthcoming dynamo experiment at HZDR.

II. KINEMATIC APPROACH

A. Setup & Equations

Initially, we focus on the kinematic problem, where only the magnetic induction equation is solved and a time-independent velocity field is prescribed, which is supposed to represent the mean (time-averaged) velocity in the experiment. The main finding from this model is a value for the critical magnetic Reynolds number, which is related to the minimum amplitude of the velocity field required for a dynamo to occur. The kinematic approach does neither consider the back-reaction of the magnetic field on the fluid flow via the Lorentz force so that we have no possibility for any saturation, nor the impact of small-scale fluctuations that could hamper (turbulent diffusion) or support (α -effect) the dynamo process.

We calculate the temporal evolution of the magnetic flux density \mathbf{B} (in the following called 'magnetic field') by numerically solving the magnetic induction equation, which reads

$$\frac{\partial \mathbf{B}}{\partial t} = \nabla \times \left(\mathbf{u} \times \mathbf{B} - \frac{1}{\text{Rm}} \nabla \times \mathbf{B} \right). \quad (1)$$

In Eq. (1) \mathbf{u} represents the velocity field and $\text{Rm} = \Omega_c R^2 / \eta$ is the magnetic Reynolds number defined with the angular velocity Ω_c of the cylinder with radius R and the magnetic diffusivity η , which is related to the electrical conductivity σ by $\eta = (\mu_0 \sigma)^{-1}$ (see also Figure 1a).

In all cases, the inner region of the simulation domain consists of a cylindrical container with radius $R = 1$ and height $H = 2$ (in dimensionless units) which is filled with an electrically conducting fluid with a magnetic diffusivity $\eta_{\text{fl}} = 1$. The fluid flow \mathbf{u} is prescribed by the data taken from hydrodynamic simulations presented in Pizzi *et al.*¹³, Giesecke *et al.*¹⁵, Pizzi, Giesecke, and Stefani²³. In these studies, it is found that the flow in a cylinder emerging at a large nutation angle can be represented by the time-averaged flow with a few large-scale inertial waves that capture the major part of the kinetic energy of the flow. A more detailed prescription of the structure of the flow field is given in the following subsection.

The flow fields used in this study are derived from hydrodynamic simulations with the spectral element code SEMTEX^{24,25}. A detailed description of the flow field as a function of the precession ratio defined by $\text{Po} = \Omega_p / \Omega_c$ can be found in^{13–15,23}. In the following, we briefly summarize the main properties that are relevant for our present study. The flow in a cylinder precessing at a large nutation angle can be characterized by three regimes. In all cases, it

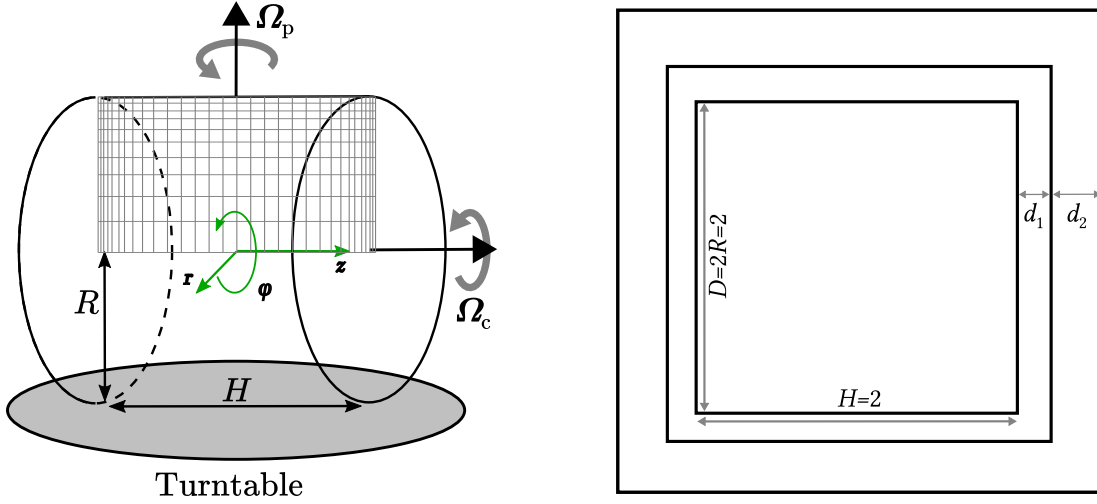


FIG. 1. (a) Sketch of the setup labeling rotation and precession axis. (b) Geometric setup for the various kinematic models. The inner cylinder with height $H = 2$ and diameter $D = 2R = 2$ frames the flow active volume, the intermediate cylinder models the container wall, and the very outer layer represents an outer volume with low electrical conductivity that resembles the laboratory exterior.

is possible to represent the time-averaged flow with a few large-scale inertial waves that capture the major part of the kinetic energy of the flow. The structure of the time-averaged flow fields as applied in the kinematic model is shown in Figure 2 for three precession ratios $Po = 0.03, 0.1, 0.2$ that are characteristic for the three flow regimes. In the subcritical regime, the flow is essentially laminar, and the geometry can be described by the superposition of the rotational motion due to the rotating cylinder and the directly driven flow (essentially an $m = 1$ mode proportional to $\cos \varphi$, see left column in Figure 2). Overlaying this is the zonal flow maintained by the cylinder's rotation (geostrophic and axisymmetric). Without precession, this would be a pure solid-body rotation with $u_\varphi \hat{e}_\varphi = f(r) \hat{e}_\varphi$ with $f(r) = r\Omega_c$ but due to the influence of precession the radial profile $f(r)$ of the zonal flow undergoes a significant modification which leads to a significant deceleration of the fluid rotation in the bulk (see bottom row in Figure 2). For larger forcing the flow transients into a supercritical region, in which the large-scale flow in the inner region has almost completely stopped so that the fluid essentially performs small-scale turbulent fluctuations and large-scale components are then only found near the walls of the container (see right column in Figure 2). These two regimes are linked by a transition zone, which is characterized by an intermittent behaviour

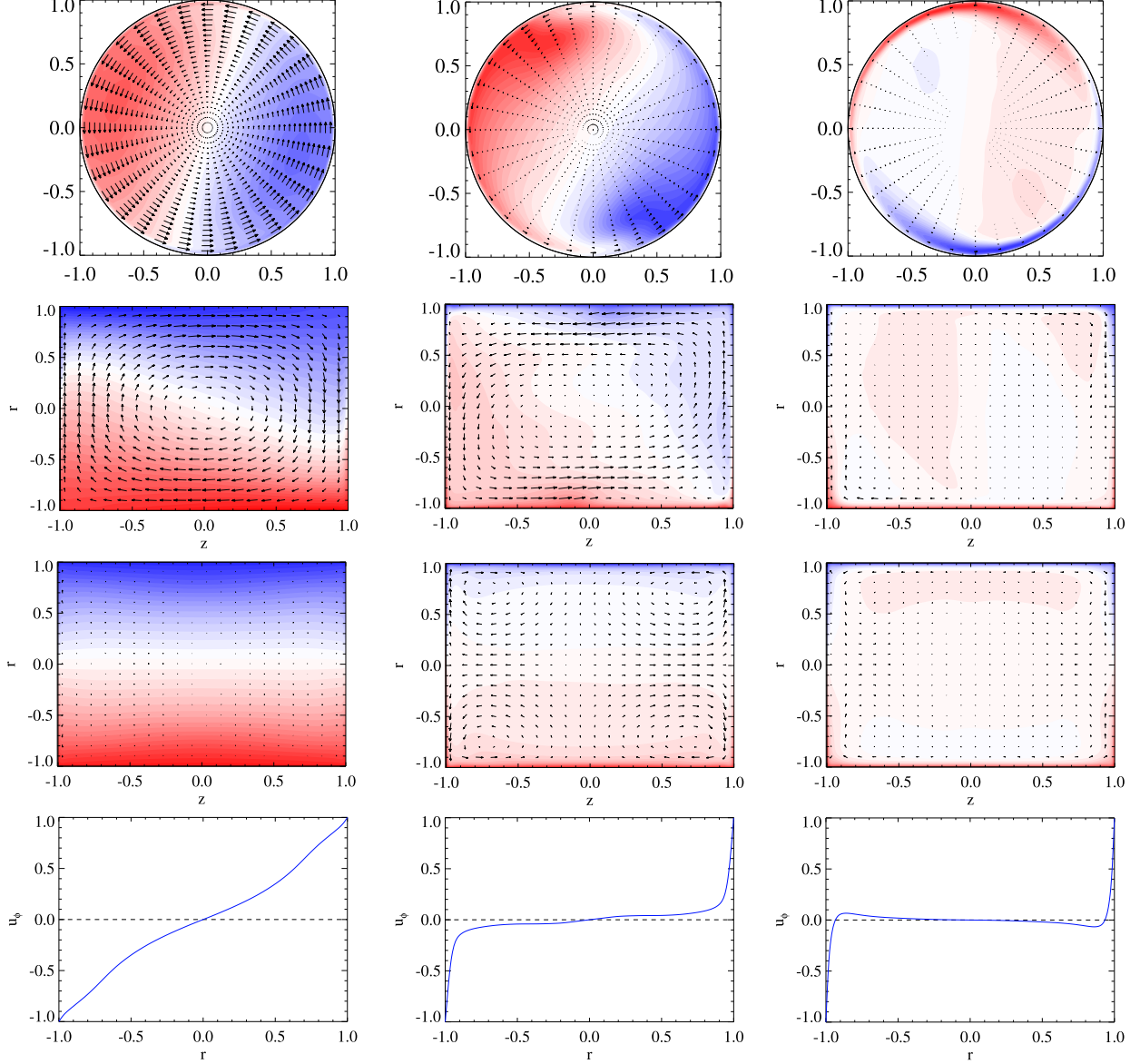


FIG. 2. Characteristic structure of the velocity field for $\text{Re} = 10^4$ and $\text{Po} = 0.03, 0.1, 0.2$ (from left to right). From top to bottom: Total flow in the equatorial plane (colors: u_z , vectors: $u_r \mathbf{e}_r + u_\varphi \mathbf{e}_\varphi$), total flow in the meridional plane where u_z is maximum (colors: u_φ , vectors: $u_r \mathbf{e}_r + u_z \mathbf{e}_z$), axisymmetric flow (again colors: u_φ , vectors: $u_r \mathbf{e}_r + u_z \mathbf{e}_z$, note the presence of the double roll mode for $\text{Po} = 0.1$ in the central column), and radial profile of the axisymmetric angular velocity $u_\varphi^{m=0}$ in the central plane.

of the large-scale flow with elements from both regimes. In this transitional region, there exists an additional large-scale contribution in the form of a double roll pattern as shown in

the central column of Figure 2 (third row).

B. Code

1. Algorithm

Assuming a prescribed time-independent flow field, Eq. (1) specifies a linear problem and the solution follows $\mathbf{B}(\mathbf{r}, t) \propto e^{\kappa t}$ with the complex eigenvalue κ consisting of the growth rate (real part γ) and the frequency (imaginary part ω). In order to solve Eq. (1) numerically, we use a finite volume approach in cylindrical coordinates. The scheme applies the constraint transport method to guarantee divergence-free solutions and is described in more detail in Giesecke, Stefani, and Gerbeth²⁶. Extensive tests of the algorithm, in particular the impact of locally varying material properties, such as electrical conductivity and comparison with an alternative approach based on Spectral/Finite Elements (the SFEMaNS code) can be found in Giesecke *et al.*²⁷.

2. Boundary conditions

We apply pseudo-vacuum conditions for the magnetic field, which read $(\mathbf{B} \times \mathbf{n})_{bc} = 0$, where \mathbf{n} is the unit normal vector at the boundary so that the tangential components of the magnetic field at the outer boundary vanish. It is well known that pseudo-vacuum conditions in kinematic models usually underestimate the critical magnetic Reynolds number that must be exceeded for the dynamo to start. The reduction depends on the geometry, i.e. essentially on the aspect ratio, and amounted, for example, to up to 30% in the kinematic models of the VKS dynamo compared to insulator boundary conditions²⁷. Nevertheless, we must restrict ourselves to the application of pseudo-vacuum conditions at the outer boundary of our system, because the strong shear near the outer boundaries enforces a high spatial resolution, which rules out the application of the Boundary-Element-Method (BEM, see e.g. Giesecke, Stefani, and Gerbeth²⁶) for the consideration of insulating boundary conditions, as this method requires a large fully populated matrix to be kept in the memory. The size of this matrix scales with N^2 , where N represents the number of grid points on the cylinder surface so that even current computers with a memory capacity of more than 1 TB are not sufficient to calculate the corresponding models. Instead, we estimate the impact of the

magnetic boundary conditions employing various setups with one or two outer layers with thickness d_1 and d_2 as sketched in Figure 1. The underlying idea is that a sufficiently thick boundary layer with poor electrical conductivity (large magnetic diffusivity) provides a good shielding of the inner volume filled with the electrically conductive fluid so that the actual nature of the electrical boundary conditions sufficiently far away from the induction region is no longer important.

We examine three different geometric configurations. Initially we revise the results for a setup that considers only the fluid interior (i.e. $d_1 = 0, d_2 = 0$). The second case examines the impact of a container wall with different values of the magnetic diffusivity (i.e. $d_1 \neq 0, d_2 = 0, \eta_w = 1 \dots 8$) and two different values for the thickness d_1 of the wall layer. In the thin layer model we use $d_1 = 0.05$ with a resolution of 5 grid cells and in the thick layer model we use $d_1 = 0.25$ with a resolution of 25 grid cells, whereby the magnetic diffusivity in the outer layer remains fixed at the maximum value of $\eta_w = 8$. Finally, in the fourth model we again apply a thin cylinder wall with $d_1 = 0.05$ and add a second outer (non-rotating) layer with $d_2 = 0.25$ and $\eta_w = 8$, which is supposed to resemble a non-conducting exterior.

C. Results of the kinematic models

1. General overview

Previous kinematic models demonstrated that dynamo action is most effective when utilizing flow from the transitional region between the subcritical and supercritical states. A detailed investigation of which components of this realization are of decisive importance for the dynamo effect was carried out in Giesecke *et al.*²² and showed that shear adjacent to the sidewall plays an important role as well as the presence of the double roll mode (DRM) which seems to be responsible for the considerable drop in the critical magnetic Reynolds number.

2. No outer layers

The typical behavior of the temporal evolution of the magnetic energy $E_m = 1/2 \int \mathbf{B}^2 dV$ is shown in Figure 3a. Here we focus on two paradigmatic cases with the flow obtained at $Po = 0.1$ scaled to a magnetic Reynolds number of $Rm = 450$ (red curve) and $Rm = 500$

(blue curve), which is slightly below and above the dynamo threshold. A striking feature is the oscillating behavior of the energy, which is superimposed on the exponentially growing part. The oscillating character of the solution can be clearly seen in the animation, which can be found in the supplementary material to this study²⁸. A systematic study of the impact of the velocity fields obtained at different Po the critical magnetic Reynolds number required for the onset of dynamo action which is shown in Figure 3b. We do not find any dynamos (at least up to $Rm = 5000$) for the flow fields in the laminar regime (i.e. below $Po \approx 0.095$). The lowest possible magnetic Reynolds number, is $Rm^{\text{crit}} \approx 450$, which is obtained for the flow field from hydrodynamic simulations at $Po = 0.1$. It is remarkable, that we find a significant smaller value for Rm^{crit} in the range $0.095 \lesssim Po \lesssim 0.11$ than above, which coincides exactly with the transition regime of the velocity field from the subcritical to the supercritical state. We therefore assume that the axially symmetric double roll occurring exclusively in this parameter range plays a significant role for the onset of dynamo action at comparatively small magnetic Reynolds numbers.

3. *Thin outer layer*

In the following we focus on the velocity field that provides the minimum critical magnetic Reynolds number in our first models so that all results discussed for the kinematic approach in the remainder of this study are calculated from the velocity field obtained at $Po = 0.1$ (central column in Figure 2). We continue with the setup that considers an additional outer layer with thickness $d_1 = 0.05$ with increased magnetic diffusivity η_w that emulates the container wall. If we look at the temporal development of the magnetic energy and its spatial distribution, we recognize two different types of dynamo action. If the wall diffusivity is close to that of the fluid (i.e. $\eta_w \lesssim 2$), a dynamo only occurs at very large Rm ($Rm^{\text{crit}} \approx 3750$). This dynamo is time-independent (no oscillatory components, see orange and green curve in Figure 4a) and the associated field energy is essentially concentrated in a narrow region near the end caps (see iso-surfaces in Figure 4c). If the outer layer has an η_w larger than $\eta_w = 2$ (see blue curve in Figure 4b), we obtain an oscillating solution that already emerges at much smaller Rm , which is exemplified by the blue curve for $\eta_w = 8$ in Figure 4a. In that case the magnetic field energy is widely distributed throughout the entire volume (however still with a characteristic pattern, see Figure 4d.) The impact of

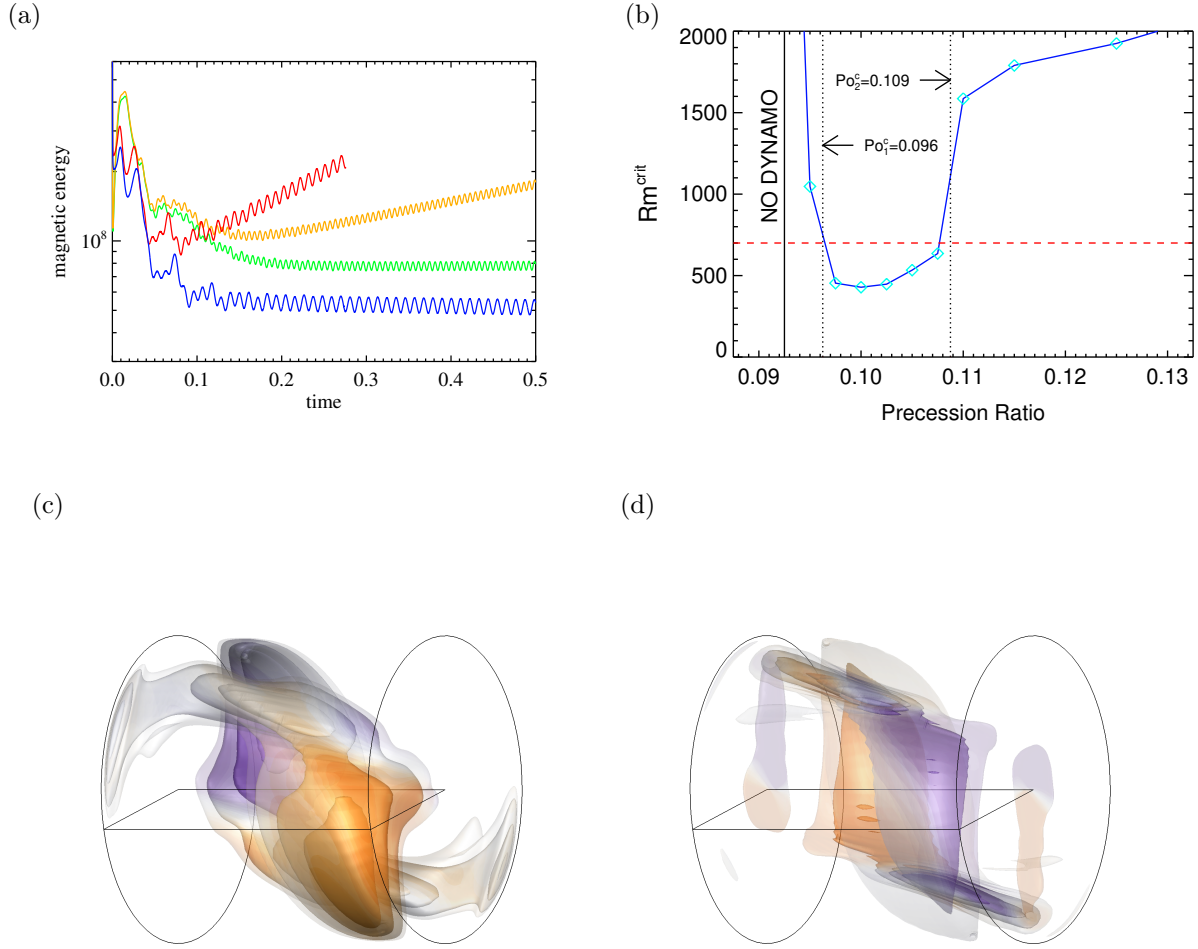


FIG. 3. (a) Magnetic energy versus time for two particular cases with $Rm = 450$ (blue) and $Rm = 500$ (red) obtained with the flow field at $Po = 0.1$ and for $Rm = 1900$ (green) and $Rm = 2100$ (orange) obtained with the flow field at $Po = 0.125$. (b) Critical magnetic Reynolds number required for the onset of dynamo action using time-averaged flow fields from hydrodynamic simulations at $Re = 10^4$. The dotted vertical lines denote the regime with a significant contribution of the double-roll mode and the horizontal red line denotes the upper limit for Rm in the planned experiment at HZDR. (c) Nested iso-surfaces of the magnetic energy at 15%, 30% and 50% of the maximum value for the flow field taken at $Po = 0.10, Rm = 500$ (d) same as (c) but for the flow field taken at $Po = 0.125$ and $Rm = 2100$. Both plots, (c) and (d) are snapshots from an oscillatory state. The corresponding animation movie can be found at²⁸.

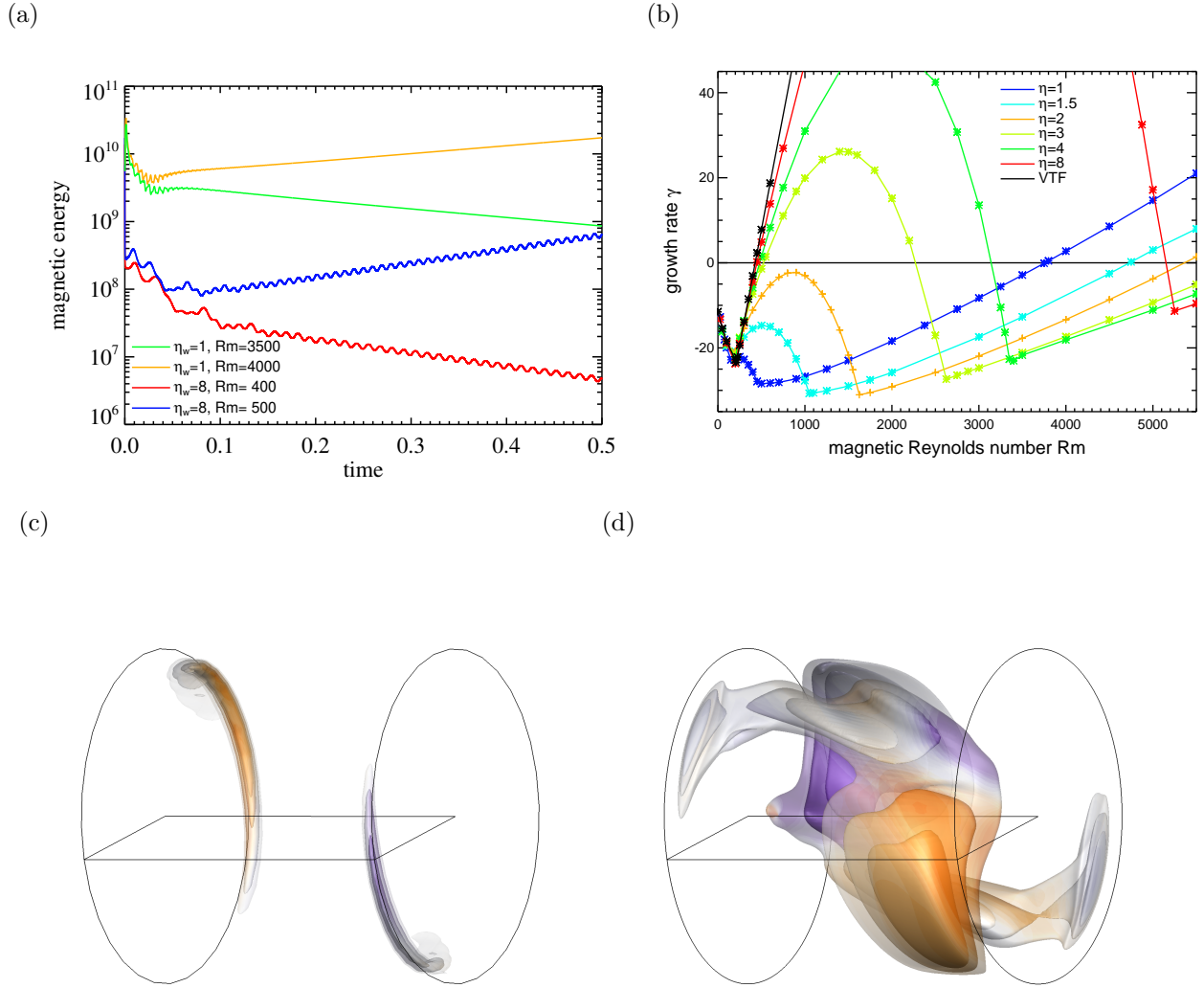


FIG. 4. (a) Magnetic energy versus time for thin outer layer with $\eta_w = 1$ (same as fluid, red and blue) and $\eta_w = 8$ (green and orange). In both cases the evolution around the onset of dynamo action is shown. (b) Growth rates γ of the magnetic field for the time-averaged flow obtained at hydrodynamic simulations at $Re = 10^4$ and $Po = 0.1$ with various values of the magnetic diffusivity related to the container walls. The black curve denotes γ for setups with vanishing tangential fields being imposed without container walls. (c) Distribution of magnetic energy for a thin layer solution with $\eta_w = 1$ and $Rm = 4000$ corresponding to the orange curve in plot (a). The nested isosurfaces represent the magnetic energy at 15%, 30% and 50% of the maximum value. The colored mapping denotes the radial field B_r . (d) Same as plot (c) but for a thin layer with $\eta_w = 8$ and $Rm = 500$ corresponding to the blue curve in plot (a). Note that this solution exhibits an oscillatory behaviour which can be seen in the related animation in the supplementary material²⁹.

the outer layer is illustrated by the growth rates shown in Figure 4b. When the magnetic diffusivity of the outer layer is increased to emulate the effect of a stainless steel container, an eigenmode is excited, the growth rates of which are represented by the inverted parabola in the individual curves in Figure 4b. This special shape results in positive growth rates for $\eta_w \gtrsim 2$ and for further increasing diffusivities the behaviour increasingly approaches that of pseudo-vacuum boundary conditions without outer layer (see black curve). It is therefore the eigenmode that belongs to the inverse parabolic growth rate, which corresponds to a dynamo that occurs at relatively low Rm achievable in the experiment, and causes a magnetic field that permeates the entire volume. Interestingly, this eigenmode belongs to an oscillating dynamo while the much less efficient dynamo is stationary, although the opposite behavior is generally assumed ³⁰.

4. *Thick outer layer*

The beneficial effect of the outer layer with sufficiently large diffusivity vanishes, when its thickness d_1 is increased, as can be recognized in Figure 5a which shows the evolution of the magnetic energy for $d_1 = 0.25$ while the magnetic diffusivity remains at $\eta_w = 8$. Here we end up with a critical magnetic Reynolds number slightly above $Rm^{\text{crit}} \approx 3000$ and the solution is again characterized by a non-oscillatory behaviour with the magnetic energy constraint to two small sections close to the endcaps, which clearly indicates that we are in the low efficiency branch (see Figure 5c). Obviously, the dominant solution in this case is again given by the less efficient branch.

Nevertheless, the highly efficient branch can be achieved again by assuming a more realistic configuration, where the container wall is emulated by a thin co-rotating layer with $d_1 = 0.05$, while the *laboratory* is modeled by a thick outer layer with $d_2 = 0.25$ large diffusivity $\eta_e = 8$ (actually, this should be an insulator in order to emulate air). In this case, we obtain an oscillating solution that occupies the entire cylinder volume and has a similar structure as in the case of the thin layer or pseudo-vacuum boundary conditions without an outer layer (see Figures 5b and 5d). However, the critical magnetic Reynolds number of $Rm^{\text{crit}} \approx 1350$ is then about two and a half times as large as in these cases.

Thus we see from the kinematic linear models that there are two different branches of dynamo solutions, the realization of which depends on the configuration of the outer boundary

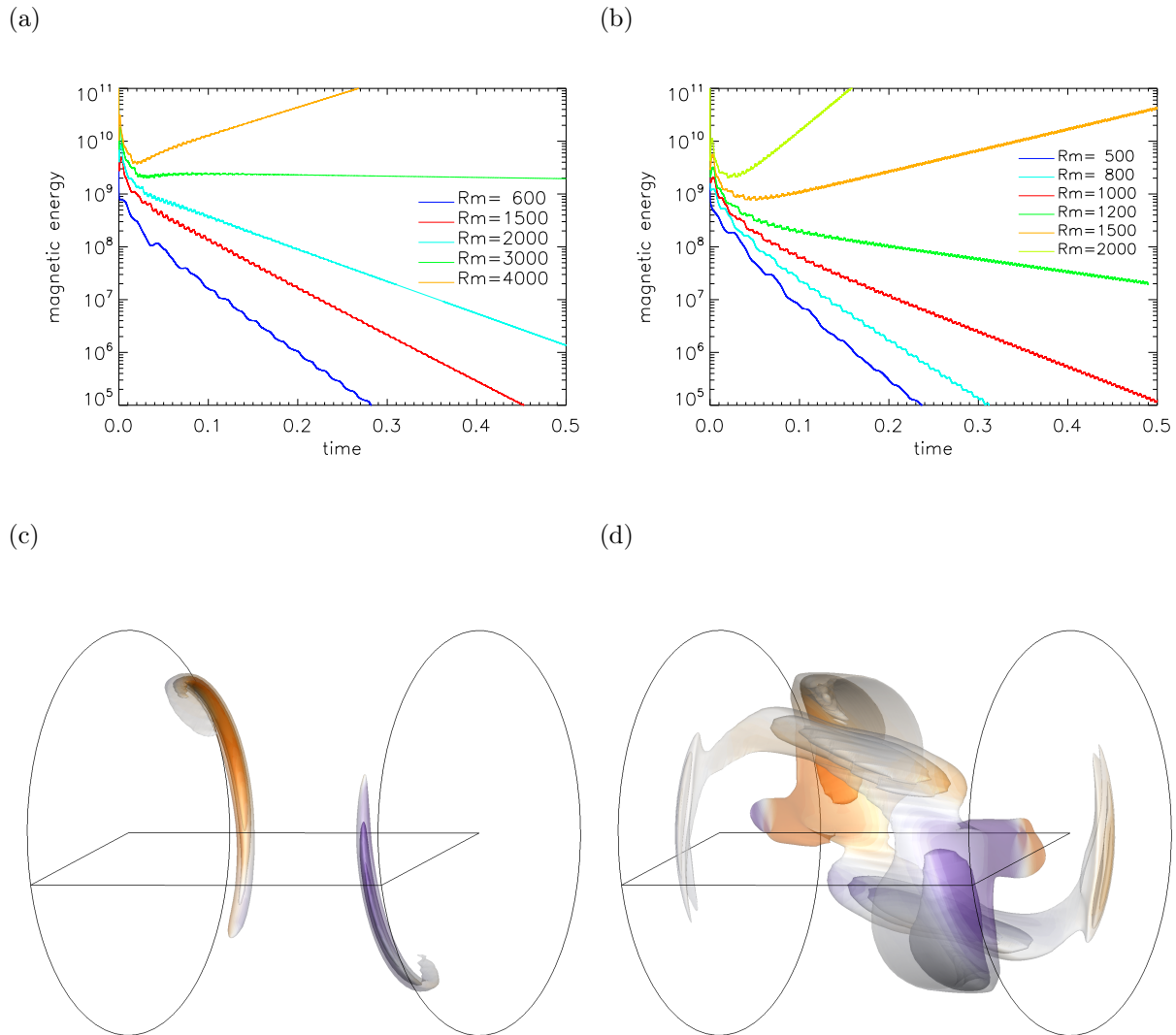


FIG. 5. (a) Magnetic energy versus time for the setup with thick container wall ($d_1 = 0.25, d_2 = 0$). (b) Same as (a) for setup with thin outer wall and stagnant outer layer ($d_1 = 0.05, d_2 = 0.25$). (c) isosurfaces for thick layer with $\eta_w = 8, Rm = 3000$ (green curve in (a)), (d) thin wall with $\eta_w = 8, Rm = 1500$, outer resting layer (orange curve in (b)).

regions, i.e. essentially on the boundary conditions. We have not investigated here at which exact parameters the transition from one branch to the other takes place, since the experimental realization must in any case start from a basically infinitely large outer volume of an insulator, namely the air in the laboratory. Interestingly, the resulting critical magnetic Reynolds number of $Rm^{\text{crit}} \approx 1350$ is very close to the value derived by Goepfert and Tilgner²⁰ for the precession dynamo with the help of simulations in a cube.

In the following, we now want to solve the induction equation coupled to the Navier-Stokes equation with a comparable setup in a self-consistent MHD model, so that the time evolution of magnetic field and velocity field is solved simultaneously, including the feedback via the Lorentz force.

III. FULL SET OF MAGNETOHYDRODYNAMIC EQUATIONS

A. Code scheme

An extension of the kinematic problem arises when we additionally consider the temporal evolution of the flow field. In this case, the Navier-Stokes equation needs to be solved as well, which in the case of precession-driven flow takes the form

$$\frac{\partial \mathbf{u}}{\partial t} = -\mathbf{u} \cdot \nabla \mathbf{u} - \nabla p + \frac{1}{\text{Re}} \Delta \mathbf{u} - 2(\text{Po} \mathbf{k}_p \times \hat{\mathbf{z}}) + (\nabla \times \mathbf{B}) \times \mathbf{B} + \text{Po} \sin \alpha r \cos(\varphi + t) \hat{\mathbf{z}}. \quad (2)$$

In addition to the terms commonly encountered in regular flow problems describing nonlinear interactions and dissipation, we have three contributions: the Coriolis force due to rotation, the Lorentz force due to the interaction with the magnetic field, and the Poincaré force accounting for acceleration due to perpetual change of the orientation of the cylinder's axis of rotation. A detailed derivation of the Navier-Stokes equation for a precessing system is given e.g. in Tilgner¹⁷.

We conduct direct numerical simulations (DNS) of the coupled system of equations (1) and (2) using the code `SpecDyn`^{14,31}, which is based on a pseudo-spectral Fourier approach. The drawback of this approach is the requirement of periodic boundary conditions in all three directions. Since this rules out an application of a cylindrical geometry, the scheme is complemented by a direct forcing immersed boundary method (IBM) which allows the consideration of nearly arbitrary shaped boundaries that prescribe the confinement for the fluid flow when the boundary conditions on these boundaries are of no-slip type. The code is parallelized using a slab decomposition and a standard MPI library. Since the most important part of the calculations results from the computation of the Fast Fourier Transformation (FFT), special efforts are undertaken to apply an extremely efficient scheme. The fulfilment of the divergence-free condition for the velocity field is ensured using a standard Pressure-Corrector method where the pressure serves as a Lagrangian multiplier so that $\nabla \cdot \mathbf{u} = 0$ is ensured (i.e. first, solve Equation (2) without pressure, then project the intermediate

solution on the divergence-free space by calculating the necessary pressure field). The same scheme is also applied to the magnetic field to ensure that the solution of the induction equation is also divergence-free as required by Maxwell's equations. The code has been tested with various configurations that proved accurate solutions with excellent convergence properties and nearly perfect strong scaling properties. A detailed description is given in Wilbert, Giesecke, and Grauer¹⁴ and a comparable approach was used for numerical models of the VKS dynamo^{32,33}.

B. Model set-up

We consider a set-up given by a cylindrical fluid region with radius $R = 1$ and height $H = 2$ embedded in a Cartesian domain with a edge length $L = 3$ so that the size of the box provides sufficient space to let the magnetic field decline outside the cylindrical vessel. The cylindrical vessel is implemented by imposing internal conditions on the fluid that emulate the (virtual) container walls by enforcing no-slip conditions at the surface of the container applying the direct forcing immersed boundary method and we do not model any special region representing the wall of the vessel because of such a layer would not be properly resolved. Instead we use a magnetic diffusivity $\eta_{\text{fl}} = 1$ for the fluid region, whereas the 'non-liquid' region outside the vessel has a magnetic diffusivity $\eta_e = 10$, which is supposed to emulate an electrically isolating exterior. The simulations are carried out with a Reynolds number of $\text{Re} = 6400$ which is the maximum possible at the resolution of $N = 256^3$ that still sufficiently resolves the boundary layers at the fluid-wall interface of the vessel³¹.

C. Results

Similar to the procedure in the kinematic case, the Poincaré number Po is varied, whereby different magnetic Reynolds numbers are considered, beginning with high values. If a positive mean growth rate is found for a particular set of parameters, further runs are executed consecutively lowering the value of Rm until no more dynamo action can be observed. Rather similar to the kinematic models we find a limited range for the preferred occurrence of a dynamo in the interval $0.105 \lesssim \text{Po} \lesssim 0.125$. However, the critical magnetic Reynolds number is significantly higher with a minimum value of $\text{Rm}^{\text{crit}} \approx 5600$ for $\text{Po} = 0.11$. The slightly

larger value for the optimum Po compared to the kinematic models can be explained by the (slightly) smaller Re (see also¹⁵). In the following we focus on the particular case Po and Rm = 6500 and compare the properties of this DNS solution with the kinematic approximation obtained at Po = 0.10 and Re = 10000. This paradigmatic examples well characterize the solution and allow a faster growth with shorter time period until a statistically steady state, while showing similar qualitative behavior as the dynamos found very close to the threshold. Here we focus on this particular Po and compare the properties of this DNS solution with Po = 0.10 and Re = 10000 in the kinematic approximation.

1. Temporal evolution of the kinetic energy

The temporal evolutions of kinetic and magnetic energy are displayed in Fig. 6, where the kinetic and the magnetic energy are defined as

$$E_m = \frac{1}{2L^3} \int_{L^3} |\mathbf{B}|^2 dV \text{ and } E_k = \frac{1}{2L^3} \int_{L^3} |\mathbf{U}|^2 dV. \quad (3)$$

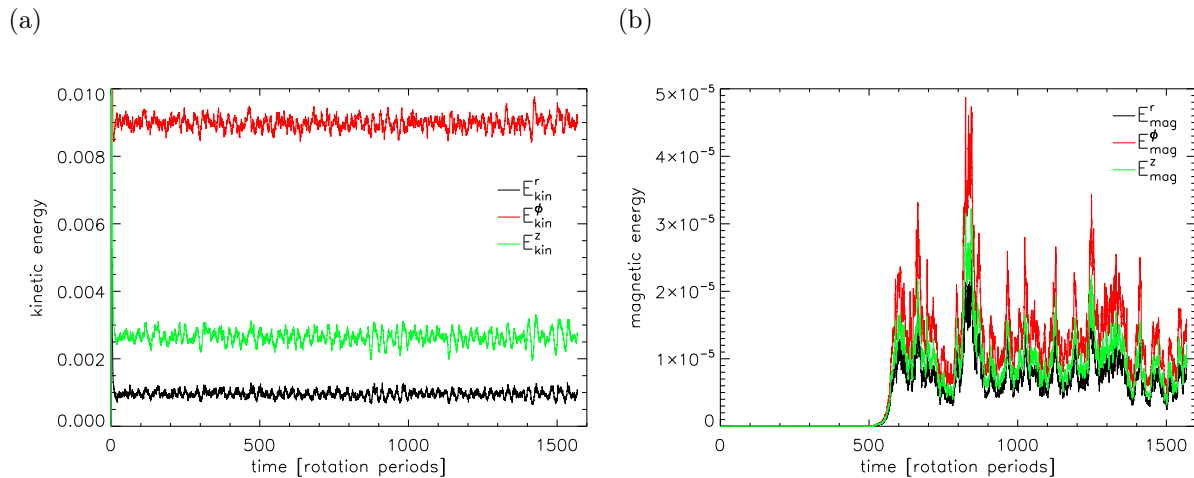


FIG. 6. Temporal evolutions of the kinetic (a) and magnetic (b) energy for Re = 6400, Rm = 6500 and Po = 0.11.

The simulations start with the pure hydrodynamic case and the effects by magnetic induction are switched on at $t = 300$. After a short initial phase the magnetic energy begins to grow for about 100 cylinder rotations and finally goes into saturation. The induced magnetic energy

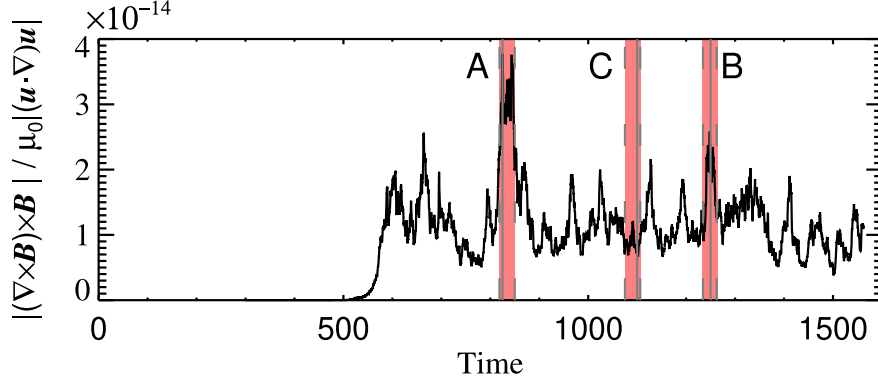


FIG. 7. Interaction parameter showing the bursts of magnetic energy in comparison with the kinetic energy. The vertical lines mark the time steps as visualized in Figure 8 and the shaded area shows the period for which animations are available in the supplementary data of this study²⁹.

E_m is much smaller than E_k and both energies are dominated by the contributions from the φ components. We find that, even in the saturated state, the presence of the magnetic field does not substantially alter the structure and the amplitude of the fluid flow via the Lorentz force. A striking property is that unlike the kinetic energy, which remains relatively steady, the magnetic energy is characterized by quasi-periodic peaks where its value suddenly rises 3 to 5 times above the average.

Although there are no substantial changes in the flow field due to the back-reaction of the magnetic field, the bursts can be clearly assigned to corresponding peaks in the interaction parameter ζ , which compares the amplitude of the Lorentz force to the inertial term in the Navier-Stokes equation:

$$\zeta = \frac{|(\nabla \times \mathbf{B}) \times \mathbf{B}|}{|\mu_0(\mathbf{u} \cdot \nabla) \mathbf{u}|} \quad (4)$$

which in case of a dynamo follows $\sim B^2/U^2$ Miralles, Plihon, and Pinton³⁴. The behavior of the interaction parameter in Figure III C 1 again clearly shows the irregular occurrence of the magnetic bursts, but also that the influence of the magnetic field remains small even in the case of a burst. In the following, we discuss three characteristic periods as marked in Figure III C 1.

2. *Dynamo bursts and field structure*

The peaks in the magnetic energy are always associated with a very strong concentration of magnetic energy in the form of local patches, as can be seen in the three-dimensional representation (see Fig 8). These patches are short-lived despite the strong concentration of magnetic energy, and even if they appear regularly, no corresponding period can be assigned. The field structure obtained from the simulations is visualized in Figure 8 which shows nested isosurfaces of the magnetic energy density for a couple of typical snapshots. We find a small scale field in terms of seemingly randomly distributed in space and time. The magnetic field patches are slightly elongated in the azimuthal direction (which goes along with the decrease of the scale in the perpendicular direction) and in general we find a spatial scale of the order of the energy carrying turbulence. The magnetic field patches exhibit an intermittent character and the thickness of the structures at least in one dimension is determined by the resistive scale. Due to the special structure of the Poincare force and the associated mean flow in the form of a standing forced inertial wave, we are not dealing with an isotropic, homogeneous turbulence, so that Kazantsev's theory (see e.g.?) is not directly applicable.

Let us label the second (major) peak as case A, the third peak as case B, and the non-peak solution as case C (see Fig. 6). The magnetic field is small-scale in all cases, whereas the velocity field is large-scale. Although our self-exciting dynamo is small-scale, ongoing hydromagnetic processes tend to excite larger scales (i.e., a large-scale magnetic field), as seen in Figure 8a. and 8b. However, these large-scale magnetic field structures are quite isolated; they do not extend throughout the entire volume and quickly dissipate due to strong magnetic diffusion, typically within 1-2 rotation periods.

In contrast, the velocity field is large-scale, characterized by two vortex structures near the cylinder wall, and is concentrated mainly near the cylinder boundary, while it is almost zero in the central volume due to the dominance of the U_φ component. The vorticity, $\boldsymbol{\omega} = \nabla \times \mathbf{U}$, naturally follows the velocity characteristics, being concentrated at the cylinder's border and negligible toward the central volume, as shown in Fig. ???. The velocity field remains largely unchanged in cases A and B, retaining characteristics similar to those in case C. The vorticity, however, penetrates slightly deeper into the central volume compared to case C (see Fig. ???), which represents the standard off-peak solution, where the magnetic field is

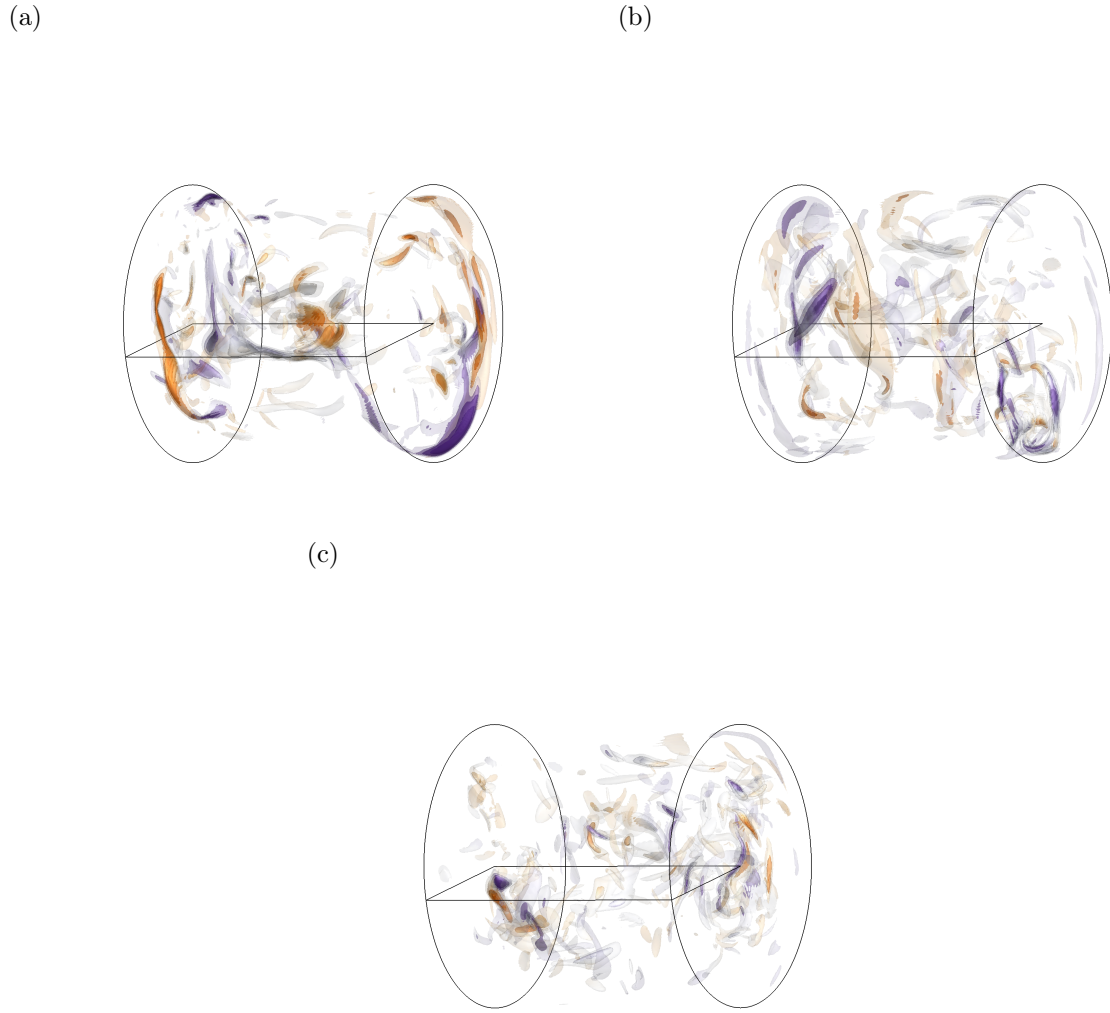


FIG. 8. Snapshot of the magnetic energy at 5%, 15%, 30%, and 50% of the respective maximum value. Top row: Snapshots for the burst peaks A and B, bottom row: snapshot for a typical case without peak. The color codes represent the radial component of the magnetic field.

weak and small-scale without any significant large-scale structures.

While the distribution of the magnetic energy in individual snapshots appears to be largely chaotic (with the exception of the bursts), this is no longer the case when we look at the time average in the turntable system. With sufficiently long averaging of more than 200 rotation periods, we get the distribution shown in Figure 9.

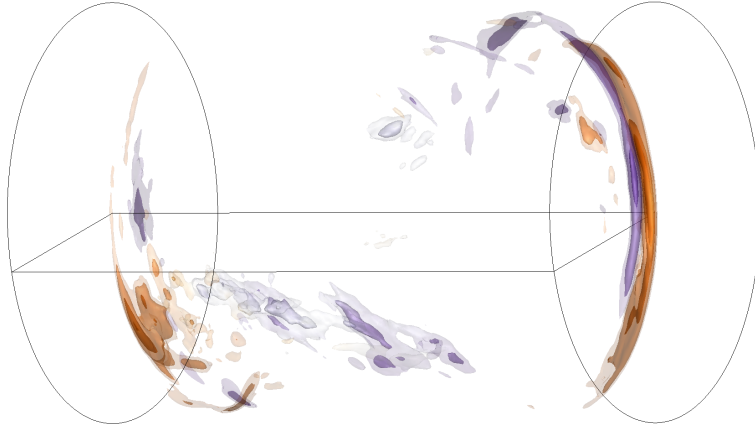


FIG. 9. Time averaged iso-surfaces of the magnetic energy. The colors denote the radial magnetic field component similar to the kinematic cases shown in figures 3c and 4d.

3. *Backreaction and kinetic power spectrum*

A reduction in the speed amplitude is also not absolutely necessary, because the dynamo that sets in is a small-scale dynamo. For this case, theoretical considerations have shown that (in a mean-field model) the feedback effect via the Lorentz force corresponds to an increased diffusivity or hyperdiffusivity $\propto \mathbf{B}^{435}$. However, a reaction of the fluid flow can be seen in a subtle way when looking at the temporal power-spectra of kinetic energy. Figure 10 compares the temporal Power-spectrum of the kinetic energy for the hydrodynamic case (left panel) with the spectrum for the dynamo case (right panel). We see that, in the hydrodynamic case, the contributions to high frequencies by the axial component z (spectral index $\alpha_{\parallel} = -2.9$) drop significantly faster than the contributions of the horizontal components r and θ (spectral index $\alpha_{\perp} \approx -1.8$). In the dynamo case, the spectral index of the horizontal components approaches $\alpha_{\perp} \approx -2.5$ which is close to the axial component, which practically does not change compared to the hydrodynamic case. This change is not particularly strong, but it is still clearly noticeable.

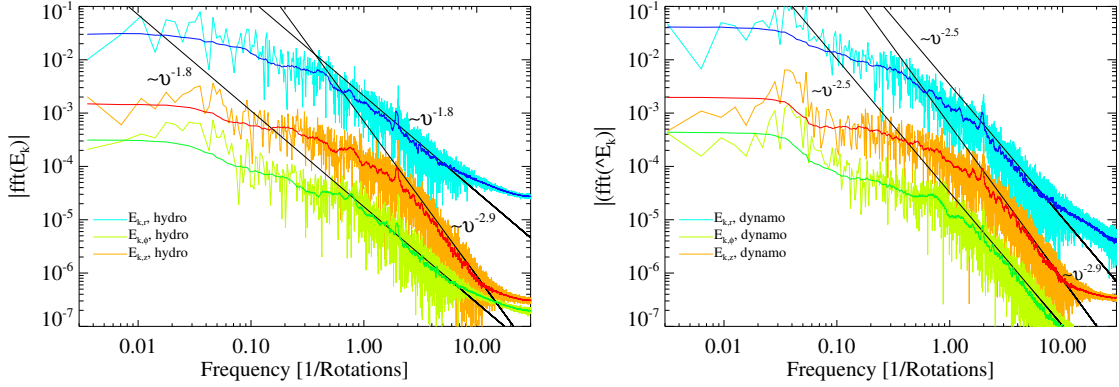


FIG. 10. Temporal power spectrum of the velocity field in the hydro case (a) and in the dynamo case (b).

IV. CONCLUSIONS

The kinematic models reveal the existence of two different branches for dynamo action. One branch is characterized by a highly localized and stationary dynamo that only occurs at rather large magnetic Reynolds number. The second type of dynamo is of oscillatory type with the magnetic field filling a larger proportion of the fluid domain. This type can occur at much lower magnetic Reynolds number, which, however requires suitable boundary conditions in terms of either a thin outer layer with large magnetic diffusivity or a comparable emulation with pseudo-vacuum BC. However, the kinematic model, which we assume best reflects the experimental setup, has a critical magnetic Reynolds number of $Rm_{\text{crit}} \approx 1300$, which is about twice as high as achievable in the planned precession dynamo experiment. Interestingly, this agrees quite well with the value derived by Goepfert and Tilgner²⁰ by means of simulations in a precessing cube.

We then applied direct numerical simulations and have calculated a comparative solution in order to investigate the time evolution of the velocity field and how it is influenced by the magnetic field through the Lorentz force and to check for consistency with the kinematic models. The configuration of this DNS essentially corresponds to that of the kinematic model, in which a stationary outer layer with large magnetic diffusivity emulates the outer space in the laboratory. Unfortunately, it is not possible to achieve the large Reynolds numbers, as they are relevant in the experiment, due to the limitations of the numerics and the hardware, respectively. This is mainly due to the extremely thin boundary layers, which

require a sufficiently high resolution. As a consequence, we find dynamo solutions in the DNS only for relatively large magnetic Reynolds numbers so that we effectively deal with a magnetic Prandtl number of the order of one with the magnetic field being small-scale and fluctuating on short time scales. At this stage it cannot be concluded with certainty that this behavior will change if we move to larger Reynolds numbers, as there are currently insufficient parameter studies available for such scaling. For the parameters considered, a small-scale burst dynamo is the typical solution. These bursts are characterized by peaks in magnetic energy, which, as previously mentioned, represent the sudden excitation of large-scale magnetic field structures. Since these structures are isolated and not sustained throughout the entire volume, they are rapidly destroyed by strong magnetic diffusion. This is followed by a period without the excitation of large-scale structures (no peaks in magnetic energy) until the hydromagnetic dynamo once again excites some large-scale magnetic field structures. Our results align with findings^{36–38}, which conclude that increasing the magnetic Prandtl number leads to a transition from large-scale dynamos to small-scale dynamos. Thus, at high values of R_m , small-scale dynamos predominate, which is consistent with our case.

To summarize, the characteristics of the magnetic fields from the kinematic simulations are clearly different from those of the DNS. However, if the magnetic field from the DNS is averaged over a sufficiently long period of time so that the occasional occurrence of the strongly localized patches is also averaged out, the structure is comparable to the structure of the weakly efficient branch in the kinematic models, which only appears at large magnetic Reynolds numbers. This explains, at least in part, the high magnetic Reynolds number required to obtain a dynamo in the DNS.

Averaging the magnetic fields over a sufficient period of time, the small scale magnetic field structures give a similar pattern as for the weak branch of the kinematic solutions, while the occasional bursts appear to have a similar character to the strong branch, but fail to establish a corresponding dynamo solution.

ACKNOWLEDGMENTS

This work benefited from support through Project Nos. GR 967/7-1 and GI 1405/1-1 of the Deutsche Forschungsgesellschaft (DFG). The authors gratefully acknowledge the Gauss

Centre for Supercomputing e.V. (www.gauss-centre.eu) for funding this project by providing computing time through the John von Neumann Institute for Computing (NIC) on the GCS Supercomputer JUWELS at Jülich Supercomputing Centre (JSC). Ján Šimkanin is grateful for support from the Alexander-von-Humboldt Stiftung (CZE 1079936).

REFERENCES

- ¹R. Stieglitz and U. Müller, “Experimental demonstration of a homogeneous two-scale dynamo,” *Phys. Fluids* **13**, 561–564 (2001).
- ²A. Gailitis, O. Lielausis, S. Dement’ev, E. Platacis, A. Cifersons, G. Gerbeth, T. Gundrum, F. Stefani, M. Christen, H. Hänel, and G. Will, “Detection of a Flow Induced Magnetic Field Eigenmode in the Riga Dynamo Facility,” *Phys. Rev. Lett.* **84**, 4365–4368 (2000).
- ³R. Monchaux, M. Berhanu, M. Bourgoin, M. Moulin, P. Odier, J.-F. Pinton, R. Volk, S. Fauve, N. Mordant, F. Pétrélis, A. Chiffaudel, F. Daviaud, B. Dubrulle, C. Gasquet, L. Marié, and F. Ravelet, “Generation of a Magnetic Field by Dynamo Action in a Turbulent Flow of Liquid Sodium,” *Phys. Rev. Lett.* **98**, 044502 (2007), [10.1103/PhysRevLett.98.044502](https://doi.org/10.1103/PhysRevLett.98.044502).
- ⁴A. Giesecke, T. Vogt, T. Gundrum, and F. Stefani, “Nonlinear Large Scale Flow in a Precessing Cylinder and Its Ability To Drive Dynamo Action,” *Phys. Rev. Lett.* **120**, 024502 (2018).
- ⁵F. Stefani, A. Gailitis, G. Gerbeth, A. Giesecke, T. Gundrum, G. Rüdiger, M. Seilmayer, and T. Vogt, “The dresdyn project: liquid metal experiments on dynamo action and magnetorotational instability,” *Geophys. Astrophys. Fluid Dyn.* **113**, 51 – 70 (2019).
- ⁶J. Léorat, “Large scales features of a flow driven by precession,” *Magnetohydrodynamics* **42**, 143–151 (2006).
- ⁷W. V. R. Malkus, “Precession of the Earth as the Cause of Geomagnetism,” *Science* **160**, 259–264 (1968).
- ⁸D. Cébron, R. Laguerre, J. Noir, and N. Schaeffer, “Precessing spherical shells: flows, dissipation, dynamo and the lunar core,” *Geophys. J. Int.* **219**, S34–S57 (2019).
- ⁹P. Olson, “The new core paradox,” *Science* **431–432**, 013008 (2013).
- ¹⁰M. Landeau, A. Fournier, H.-C. Nataf, D. Cébron, and N. Schaeffer, “Sustaining earth’s magnetic dynamo,” *Nature Reviews Earth and Environment* **3**, 255 – 269 (2022).

- ¹¹M. G. Rochester, J. A. Jacobs, D. E. Smylie, and K. F. Chong, “Can precession power the geomagnetic dynamo?” *Geophys. Journal* **43**, 661–678 (1975).
- ¹²R. R. Kerswell, “Upper bounds on the energy dissipation in turbulent precession,” *J. Fluids Mech.* **321**, 335–370 (1996).
- ¹³F. Pizzi, A. Giesecke, J. Šimkanin, and F. Stefani, “Prograde and retrograde precession of a fluid-filled cylinder,” *New J. Phys.* **23**, 123016 (2021).
- ¹⁴M. Wilbert, A. Giesecke, and R. Grauer, “Numerical investigation of the flow inside a precession-driven cylindrical cavity with additional baffles using an immersed boundary method,” *Phys. Fluids* **34**, 096607 (2022).
- ¹⁵A. Giesecke, T. Vogt, F. Pizzi, V. Kumar, F. Garcia-Gonzalez, T. Gundrum, and F. Stefani, “The global flow state in a precessing cylinder.” *J. Fluid Mech.* **XXX**, in press (2024).
- ¹⁶C. Stys and M. Dumberry, “A past Lunar dynamo thermally driven by the precession of its inner core,” *Journal of Geophysical Research: Planets* **125**, e2020JE006396 (2020).
- ¹⁷A. Tilgner, “Precession driven dynamos,” *Phys. Fluids* **17**, 034104 (2005).
- ¹⁸C.-C. Wu and P. Roberts, “On a dynamo driven by topographic precession,” *Geophys. Astrophys. Fluid Dyn.* **103**, 467–501 (2009).
- ¹⁹C. Nore, J. Léorat, J.-L. Guermond, and F. Luddens, “Nonlinear dynamo action in a precessing cylindrical container,” *Phys. Rev. E* **84**, 016317 (2011).
- ²⁰O. Goepfert and A. Tilgner, “Dyamos in precessing cubes,” *New J. Phys.* **18**, 103019 (2016), 10.1088/1367-2630/18/10/103019.
- ²¹R. F. Gans, “On hydromagnetic precession in a cylinder,” *J. Fluids Mech.* **45**, 111–130 (1971).
- ²²A. Giesecke, T. Vogt, T. Gundrum, and F. Stefani, “Kinematic dynamo action of a precession-driven flow based on the results of water experiments and hydrodynamic simulations.” *Geophys. Astrophys. Fluid Dyn.* **113**, 235–255 (2019).
- ²³F. Pizzi, A. Giesecke, and F. Stefani, “Ekman boundary layers in a fluid filled precessing cylinder,” *AIP Advances* **11**, 035023 (2021).
- ²⁴H. M. Blackburn and S. J. Sherwin, “Formulation of a Galerkin spectral element-Fourier method for three-dimensional incompressible flows in cylindrical geometries,” *J. Comp. Phys.* **197**, 759–778 (2004).
- ²⁵H. M. Blackburn, D. Lee, T. Albrecht, and J. Singh, “Semtex: a spectral element-Fourier solver for the incompressible Navier-Stokes equations in cylindrical or Cartesian coordi-

- notes,” *Comput. Phys. Cmm.* **245**, 106804–1–13 (2019).
- ²⁶A. Giesecke, F. Stefani, and G. Gerbeth, “Kinematic simulation of dynamo action by a hybrid boundary-element/finite-volume method,” *Magnetohydrodynamics* , 237 – 252 (2008).
- ²⁷A. Giesecke, C. Nore, F. Stefani, G. Gerbeth, J. Léorat, F. Luddens, and J.-L. Guermondz, “Electromagnetic induction in non-uniform domains,” *Geophys. Astrophys. Fluid Dyn.* **104**, 505 – 529 (2010).
- ²⁸A. Giesecke, “supplemental material,” www.giesecke.net (2024).
- ²⁹A. Giesecke, “supplemental material,” www.giesecke.net (2024).
- ³⁰G. Rüdiger, D. Elstner, and M. Ossendrijver, “Do spherical α^2 -dynamoes oscillate?” *Astron. Astrophys.* **406**, 15–21 (2003).
- ³¹M. Wilbert, *Implementation and application of a pseudo-spectral MHD solver combined with an immersed boundary method to support the DRES-DYN dynamo experiment*, Ph.D. thesis, Fakultät für Physik und Astronomie der Ruhr-Universität Bochum (2024).
- ³²S. Kreuzahler, D. Schulz, H. Homann, Y. Ponty, and R. Grauer, “Numerical study of impeller-driven von Kármán flows via a volume penalization method,” *New J. Phys.* **16**, 103001 (2014), [10.1088/1367-2630/16/10/103001](https://doi.org/10.1088/1367-2630/16/10/103001).
- ³³S. Kreuzahler, Y. Ponty, N. Plihon, H. Homann, and R. Grauer, “Dynamo enhancement and mode selection triggered by high magnetic permeability,” *Phys. Rev. Lett.* **119**, 234501 (2017).
- ³⁴S. Miralles, N. Plihon, and J.-F. Pinton, “Lorentz force effects in the bullard–von kármán dynamo: saturation, energy balance and subcriticality,” *J. Fluids Mech.* **775**, 501–523 (2015).
- ³⁵K. Subramanian, “Hyperdiffusion in nonlinear large- and small-scale turbulent dynamoes,” *Phys. Rev. Lett.* **90**, 245003 (2003).
- ³⁶M. Etchevest, M. Fontana, and P. Dmitruk, “Behavior of hydrodynamic and magnetohydrodynamic turbulence in a rotating sphere with precession and dynamo action,” *Physical Review Fluids* **7**, 103801 (2022).
- ³⁷K. Richardson, R. Hollerbach, and M. Proctor, “From large-scale to small-scale dynamoes in a spherical shell,” *Phys. Fluids* **24**, 107103 (2012).
- ³⁸D. Hughes, F. Cattaneo, and J.-C. Thelen, *Dynamo and Dynamics, a Mathematical Challenge*, NATO Science Series (Kluwer Academic Publishers, Dordrecht / Boston / London,

2001).